ToF-SIMS 3D Imaging of Native and Non-Native Species within HeLa Cells

Jeremy Brison[1,3,*,γ], **Michael A. Robinson**[1,2,γ], **Danielle S.W. Benoit**[3,†], **Shin Muramoto**[1,2,°],
Patrick S. Stayton[3], and **David G. Castner**[1,2,3,§]

[1]National ESCA and Surface Analysis Center for Biomedical Problems, University of Washington, Seattle, WA 98195-1653

[2]Department of Chemical Engineering, University of Washington, Seattle, WA 98195-1653

[3]Department of Bioengineering, University of Washington, Seattle, WA 98195-1653

Abstract

In this study a non-native chemical species, bromodeoxyuridine (BrdU), was imaged within single HeLa cells using time-of-flight secondary ion mass spectrometry (ToF-SIMS). Z-corrected 3D images were reconstructed that accurately portray the distribution of intracellular BrdU as well as other intracellular structures. The BrdU was localized to the nucleus of cells, whereas structures composed of $C_xH_yO_z^-$ were located in bundles on the periphery of cells. The $C_xH_yO_z^-$ sub-cellular features had a spatial resolution at or slightly below a micron (900nm), as defined by the distance between the 16 and 84% intensities in a line scan across the edge of the features. Additionally, important parameters influencing the quality of the HeLa cell 3D images were investigated. Atomic force microscopy measurements revealed that the HeLa cells were sputtered at a rate of approximately 4 nm per 10^{13} C_{60}^+ ions/cm^2 at 10 keV and a 45° incident angle. Optimal 3D images were acquired using a Bi_3^+ liquid metal ion gun operating in the simultaneous high mass and spatial resolution mode.

Introduction

Time-of-flight secondary ion mass spectrometry (ToF-SIMS) is increasingly used in the life sciences to characterize complex biological samples and biomedical devices[1–8]. This rapid expansion coincides with the advent of polyatomic ion sources, which have fundamentally changed the way ToF-SIMS data is acquired[9–11]. Compared to their monoatomic counterparts such as Bi^+, triatomic ions such as Bi_3^{q+} [12,13], as well as cluster ions such as C_{60}^{q+} [14] and gas cluster ion beam (GCIB) Ar[15–19] provide higher secondary ion yields for high mass molecular fragments which results in an extended mass range and enhanced sensitivity. The concerted action of the atoms in the clusters produced from the C_{60} and GCIB sources during impact with the surface also results in higher sputter yields[20–24], causing less residual chemical damage during analysis[25,26] due to the formation of a lower damage volume from shallower implantation depths[27]. Because of this capability, C_{60} and GCIB Ar have demonstrated a remarkable aptitude for molecular depth profiling organic and biological materials[25,28,29]. Numerous examples of successful molecular depth profiles

§Corresponding Author: David G. Castner, 1-206-543-8094 (phone), 1-206-543-3778 (fax), castner@uw.edu.
*Current affiliation: IBA Medical Accelerators Solutions, Belgium
†Current affiliation: Departments of Biomedical Engineering and Chemical Engineering, University of Rochester, Rochester, New York 14627
°Current affiliation: National Institute of Standards and Technology, Gaithersburg, Maryland 20899
γThese authors contributed equally to this work.

have been reported in the literature for polymers and biological samples (See reference [26] for a recent review).

The use of cluster ion sources in ToF-SIMS has demonstrated a great potential for molecular 3D imaging of single biological cells[30–38]. The sub-micron spatial resolution of ToF-SIMS[39,40], combined with its parallel detection capability and molecular specificity gives this technique the ability to simultaneously detect all secondary ions without the need for selective markers, making it a complementary tool to methods such as matrix-assisted laser desorption ionization (MALDI) mass spectrometry[41,42] and fluorescence microscopy[43]. Particularly intriguing is the prospect of mapping the intracellular distributions of small molecule therapeutics in single cells with ToF-SIMS, now a possibility given the advances described above. An important criterion to achieve this is a data acquisition mode that provides simultaneous high spatial and mass resolutions.

A significant number of 2D images of cells and tissues have been published in literature, but few full molecular 3D images have been reported to date. Obtaining 2D and 3D images of single cells is still challenging[4], with the main reasons stemming from the extreme surface sensitivity of the technique, low secondary ion yields (especially after prolonged sputter times) and the necessity to perform the experiment in an ultra-high vacuum environment.

C_{60} and GCIB Ar sources offer new opportunities for analysis of biological samples because they allow depth profiling with low ion induced chemical damage[4,44]. They can be used to "clean up" the sample surface[37,45,46] and to reach specific depths within the cells, which offers the opportunity to more easily control the depth analyzed in a cell than the freeze-fracture method. However, since a biological cell is a highly heterogeneous volume, it is essential to obtain a detailed and a fundamental understanding of "cluster ions – biological matter" interactions so that the optimal sample preparation (chemical fixation, freeze-dried, frozen-hydrated, freeze-fracture, etc.) and cluster cleaning can be selected to produce optimal 3D imaging. For example, the ion induced chemical damage and the etching rates in biological matter are still an area of active investigation[34,35,47]. Also, it is not clear if these parameters are constant through depth profiling and for all species present in all sample types. The sputter rate of NIH/3T3 fibroblasts using C_{60}^{++} was shown to be largely uniform throughout an entire depth profile[35], although the ion yields of many secondary ions decreased in NIH/3T3 fibroblasts[48] with increasing primary ion dose. In rat brain tissue samples the secondary ion yield of cholesterol, phospholipid and protein fragments did not decrease substantially with increasing sputter dose when the tissue was held at −120 °C, although the sputter yields were not measured[49].

Other groups have identified the importance of improving the mass resolution for ToF-SIMS, as well as acquiring data with both high mass and spatial resolutions. This is a challenge for ION-TOF and Physical Electronics instruments since they require pulsing of the primary ion beam. Using "normal" operating parameters in these instruments, spatial resolution is usually sacrificed for mass resolution, or vice versa. Two examples of instruments that circumvent this problem are a modified commercial MALDI instrument with a C_{60} primary ion source[50,51], and Ionoptika's J105 instrument[32,36]. Both of these instruments utilize a direct current instead of a pulsed primary ion beam with the objective of acquiring data simultaneously at both high spatial and mass resolutions. Due to other instrument constraints, the modified MALDI instrument was not able to achieve high spatial resolution images. A C_{60} primary ion beam was recently added to a Fourier transform ion cyclotron resonance mass spectrometer to achieve mass resolving powers greater than 3,000,000[52,53]. Although the spatial resolution demonstrated by this instrument was inferior to the spatial resolution used in typical ToF-SIMS imaging experiments, the mass resolving power is unparalleled. New combined high mass and spatial resolution imaging modes have

been recently introduced by PHI[54] and IONTOF[55]. Thus, imaging with simultaneous high mass and spatial resolution is now receiving significant interest in the ToF-SIMS community.

In this study we investigate the 2D and 3D ToF-SIMS images of human HeLa cells acquired in the dual beam mode[56] (*i.e.*, Bi_3^+ for imaging and C_{60}^+ for etching) with the sputter depth calibrated using atomic force microscopy (AFM). The HeLa cells used in these experiments were treated with bromodeoxyuridine (BrdU), a well-known nuclear marker[57], to help identify and delimit the nuclei during 3D imaging. The Bi_3^+ liquid metal ion gun (LMIG) was operated at different conditions (high mass resolution, high spatial resolution, simultaneous high mass and spatial resolutions) to assess the effectiveness of the LMIG operating mode for imaging the HeLa cells.

Materials and Methods

Time-of-Flight Secondary Ion Mass Spectrometry

ToF-SIMS experiments were performed using an ION-TOF ToF-SIMS 5–100 (ION-TOF GmbH, Münster, Germany) equipped with a Bi LMIG and a C_{60} electron impact source. A pulsed 25 keV Bi_3^+ analysis beam and a direct current 10 kV C_{60}^{q+} (q = 1, 2) sputter beam were used for this study. Both beams struck the target at an angle of 45°. The Bi LMIG gun was used in a high current, high mass resolution (HMR) mode and in two types of high spatial resolution (HSR) modes. An example spectrum for each at m/z 81$^-$ is plotted in Figure 1. The two types of HSR modes are "burst alignment" where the ion beam has a long pulse width (higher current but nominal mass, top spectrum) and "burst" mode, where the ion beam has a series of short pulses (high mass and spatial resolution but lower target current, middle spectrum). In the burst mode, the long pulses (170 ns in this study) are cut into a burst of successive short ion pulses by a sine blanker operating at 40 MHz (i.e., 6 pulses of 2 ns every 25 ns). In the burst alignment mode, the ion beam is not bunched to avoid the energy dispersion that causes the degradation of the spatial resolution. In contrast, the short pulses in the burst mode provide simultaneous high mass and spatial resolutions with a low, but useable, primary ion current (see below). Six peaks resulting from these short pulses were summed together to increase the signal intensity, providing increased sensitivity.

To acquire secondary ion images, Bi_3^+ was typically rastered over a 200×200 μm^2 area, centered inside a 500×500 μm^2 C_{60}^{q+} crater. Target currents were measured separately before each measurement in the pulsed mode for Bi_3^+ and in the direct current mode for C_{60}^{q+}. The Bi_3^+ current was 0.2 pA in the HMR mode (< 1 ns pulse width), 0.08 pA in burst alignment (100 ns pulse width), and less than 0.01 pA in the burst mode (170 ns pulse width). The C_{60}^{q+} current was between 0.15 nA and 1 nA. The Bi LMIG was operated at a frequency of 10 kHz. The mass resolutions (measured at $C_2H_3^+$, *m/z* 27$^+$) were typically >6,000 (HMR mode), nominal (burst alignment mode), and >5,000 (burst mode). The typical probe sizes of the Bi LMIG in the different operating modes were ~5 μm (HMR mode), ~200 nm (burst alignment mode), and ~200 nm (burst mode). Positive spectra produced from the Bi_3^+ primary ion beam were mass calibrated using CH_3^+, $C_2H_3^+$, $C_3H_5^+$, $C_3H_3O^+$, $C_4H_7^+$ and $C_5H_{14}NO^+$. Negative spectra produced from the Bi_3^+ primary ion beam were mass calibrated using two separate peak lists. To achieve the highest mass accuracy for the organic peaks, the spectra were calibrated with CH^-, OH^-, C_2H^-, and $C_{16}H_{31}O_2^-$. To achieve the highest mass accuracy for the inorganic peaks, the spectra were calibrated to O^-, OH^- Cl^-, and, PO_2^-. Low energy electrons were flooded onto the sample to compensate for charge buildup.

For the burst mode data set, 14 2D images (referred to as "slices") were acquired. This data was collected in the "non-interlaced" mode, where the analysis and sputter beams are active in different ToF-cycles. This operation mode is necessary to produce images with sufficient secondary ion intensities. The total Bi_3^+ accumulated ion dose for each slice was less than 7.5×10^{10} ions/cm^2. The total C_{60}^+ ion dose per slice was 1.3×10^{14} ions/cm^2, which corresponds to the removal of ~52 nm of material per slice (see below). For the HMR data set, 244 2D images were acquired. The data was collected with the Bi_3^+ and C_{60}^+ ion beams operated in the same ToF cycle (referred to as "interlaced" mode[58]). The total Bi_3^+ accumulated ion dose for each slice was 2.0×10^{10} ions/cm^2, and the total C_{60}^+ ion dose per slice was 1.3×10^{13} C_{60}^+ ions/cm^2.

Data Handling/3D Image Reconstruction

ToF-SIMS data were reconstructed in 3D using the ZcorrectorGUI[35] (Dan Graham Ph.D, NESAC/Bio, University of Washington), a free GUI that runs in Matlab (MathWorks, Natick, MA). First, peak intensity images were plotted in the SurfaceLab 6 software (ION-TOF GmbH, Münster, Germany), and then exported as .bif3D files. The .bif3D files were imported into the ZcorrectorGUI to create the 3D reconstructions.

For comparison of the 3D images reconstructed from the different modes it is best to have the same number of 2D image slices. Thus, for the burst mode images each of the 14 2D Bi_3^+ images was split into two 2D images, resulting in 28 slices. This had no effect on the resulting 3D images other than to increase the "height" of the reconstructed 3D image, which only depends on the number of slices in the stack. For the 3D HMR image, the initial 244 2D images were reconstructed by plotting 24 slices, where each new reconstructed slice was the summation of 10 2D images from the raw data. This was done to so that the reconstructed HMR 3D image would have a similar "height" to the reconstructed burst mode 3D images. The last four slices were excluded from the HMR 3D reconstruction.

Atomic Force Microscopy

AFM (Dimension 3100, Veeco Metrology Inc., Santa Barbara, CA) was used to measure the height of the cells and their morphology before and after sputtering with differing C_{60}^{q+} doses. The AFM was equipped with a 315 kHz, 42 N/m PointProbe Plus silicon tip (Nanosensors, Neuchâtel, Switzerland), and operated in the intermittent contact mode in air. At least four locations of each cell at a particular area were scanned to determine the average height. These measurements were used to calibrate the depth scale of molecular depth profiles. As a first approximation, the cells nuclei and cytoplasm were considered as flat areas and their thickness was averaged over the selected regions.

HeLa Cells and Sample Preparation

HeLa cells, human cervical carcinoma cells (ATCC CCL-2), were maintained in minimum essential media (MEM) containing L-glutamine (Gibco), 1% penicillin-streptomycin (Gibco), and 10% fetal bovine serum (FBS, Invitrogen) at 37 °C and 5% CO_2. After trypsinizing, the HeLa cells (12,000 cells/cm^2) were seeded onto Si surfaces that had been cleaned by sequential sonications in DI water, dichloromethane, acetone, and methanol. Then the cells were allowed to adhere overnight to the Si surface. The cells were then prepared for ToF-SIMS analysis in the following ways:

1. Figure 2: Cells were washed in ammonium acetate (AA), and either air dried (top row) or dried with a gentle stream of nitrogen (bottom row). The AA rinse is necessary to remove excess media which, when dried, may leave behind salt crystals that sputter very slowly with C_{60} etching.

2. Figures 3–6: Cells were washed in AA, fixed in 4% phosphate-buffered paraformaldehyde, rinsed with double distilled H_2O (ddH$_2$O), and dried with N_2. Cells were also incubated in the presence of 20 μM BrdU for 48 hours prior to seeding. BrdU, which is incorporated into DNA during cell division, is a good label for cell depth profiling. BrdU can be detected using the $^{81}Br^-$ signal ($^{79}Br^-$ overlaps with PO_3^-), as well as $C_4H_2N_2O_2Br^-$ at m/z 189 and 191 ($^{79}Br^-$ and $^{81}Br^-$ isotopes).

Results and Discussion

C_{60} etching to reveal subcellular structures

Obtaining the ideal ToF-SIMS image of a biological cell is challenging. Complexities from many factors can affect the quality of the acquired image. Sample preparation is one of these factors and numerous studies have focused on optimizing sample preparation procedures for analyzing cells with ToF-SIMS[34,48,59,60]. The general conclusion is that no single preparation procedure is optimal for all experiments, since even a small change in the preparation methods can change the quality of the information obtained from single cells. The sample preparation methods can be divided into two broad categories: those where the cell is analyzed frozen-hydrated (more difficult experimentally but produces the most native cells) and those that dehydrate the cell prior to analysis (easier experimentally). Dehydration introduces artifacts like shrinking and cracking of cells, and redistribution of lipids in the plasma membrane[34,59,60], however gluteraldehyde fixation may minimize these effects[61,62].

Figure 2 shows positive secondary ion images of HeLa cells imaged with Bi_3^+ for two slightly different preparation protocols[59,60], both of which dehydrate the cells: one in which the cells were rinsed in AA for 30 seconds and then dried in air (top row); the other where the cells were rinsed in AA for the same time but dried using a gentle stream of N_2 (bottom row).

The sum of phospholipid signals (m/z 58^+, 86^+, 125^+, 166^+, 184^+ and 224^+, See Table S-1 for details) in the third column shows that the plasma membranes of the cells dried in air retained the native cell shape better than those dried with a N_2 stream. The images in the bottom row show that the Na^+, K^+ and phospholipid signals are not specifically localized outside or inside the cells, indicating extensive damage to the plasma membrane, and therefore leakage of some internal contents for samples dried with a N_2 stream. The ions at m/z 58^+ and 86^+ may also arise from amino acids[63]. However, in the case of cells, the primary source of these ions are phospholipids. This was shown in the 3D image of a NIH/3T3 fibroblast[35], and also for the HeLa cells in this study as the images from the m/z 58^+ and 86^+ ions differed from the image of the well-known amino acid fragment $C_4H_8N^+$ at m/z 70^{+}[63] (data not shown).

One way to overcome the problem of damage or smearing introduced by the sample preparation method is to use C_{60} cluster ion etching to remove contaminants or damaged regions from the sample surface, allowing higher quality ToF-SIMS images to be acquired[37,45,46]. ToF-SIMS images of HeLa cells after C_{60}^{++} etching are also shown in Figure 2. In the fifth column, acquired after C_{60}^{++} etching, a subcellular feature of the cells is now visible: the perinuclear enriched phospholipid regions that delimit the cells' nuclei. Smaller phospholipid spots within the nucleus suggest positions of nucleoli. Using both preparation methods, intracellular structures after C_{60}^{++} etching appear similar, independent of which drying method was used. In both cases, the growth medium residues and the material located around the cells from leakage, as well as the outer cell membrane, were removed by the etching (1.0×10^{14} C_{60}^{++} ions/cm^2), revealing subcellular features. Thus, C_{60}

etching is a useful tool to reveal intracellular structures by removing the surface damage caused by non-optimal, sample preparation methods.

It is interesting that the phospholipid rich regions observed in Figure 2 and in Brison *et al.*[64] are similar to those obtained with a NanoSIMS instrument for HeLa cells fixed in gluteraldehyde and treated with an isotopically labeled peptide[65], as well as ToF-SIMS images of cells fixed with gluteraldehyde[33,61] and formaldehyde[35].

Burst mode and 3D imaging of single cells

Another factor that determines the quality of the ToF-SIMS image is sample morphology. Features such as surface roughness, chemical complexity, and heterogeneous structure of the sample can play a significant role in acquiring high resolution images. Recent reviews have highlighted that the nominal mass resolution resulting from not bunching the LMIG analysis beam in the HSR mode strongly limits the capabilities of ToF-SIMS to detect specific biomolecules due to poor mass resolution, especially those ions with inherently low intensities[32]. For example, imaging the Br^- peaks from the BrdU molecules in the HSR imaging mode is impossible because their peaks in the mass spectrum cannot be discriminated from the PO_3^- and $H_2PO_3^-$ phosphate peaks. Similarly, phospholipid, amino acid, nucleic acid and carbohydrate peaks strongly interfere with each other in spectra obtained using the HSR mode. To collect an image representative of a particular species when the analysis is done at nominal mass resolution, that species of interest must be the dominant peak at the selected nominal mass. While this happens on occasion, this is usually not the case. On the other hand, the main advantage of the ToF-SIMS technique over other imaging modalities such as MALDI mass spectrometry is its sub-micrometer spatial resolution. Preserving the mass, spatial and depth resolutions is essential for optimal 3D chemical analysis of single cells with ToF-SIMS.

In this investigation, we use the burst mode (see Methods section) to acquire ToF-SIMS images of single cells with both high mass and spatial resolutions to produce a more accurate representation of those cells. An example of negative ToF-SIMS spectra obtained with 25 keV Bi_3^+ using three different analysis modes are shown in Figure 1 for *m/z* 81^-. The figure shows that the $^{81}Br^-$ signal cannot be resolved in the HSR burst alignment mode (top spectrum), making accurate mapping of the BrdU molecule challenging since only the low signals of the molecular BrdU peaks could be used. If the m/z 81^- peak were chosen to construct an image, any signal produced by the $^{81}Br^-$ ion would be overwhelmed by the more intense $H_2PO_3^-$ peak. Conversely, the spectrum obtained in HMR bunched mode (bottom spectrum) allows the discrimination of the $^{81}Br^-$ peak from the $H_2PO_3^-$ peak, but the images produced would have poor spatial resolution (~5 μm). Lastly, the spectrum acquired in burst mode (middle spectrum) allows the proper identification of both species while preserving the spatial resolution provided by the HSR imaging mode (see below). The intensity of the $^{81}Br^-$ peak is obtained by summing the intensities of the 6 peaks created in the burst mode (see Methods section for details). Figure S-1 shows the accumulated intensities of other phosphate-containing secondary ions (PO_2^-, PO_3^-, $H_2PO_3^-$ and $H_2PO_4^-$), which confirms the identification of the $H_2PO_3^-$ ion.

Figure 3 compares the images obtained in the HMR and burst modes (top and bottom rows, respectively) from the same sample of chemically-fixed HeLa cells. The data recorded in 3D (alternate cycles of imaging with Bi_3^+ and etching with C_{60}^+) but are displayed as the sum of selected 2D images. For the burst mode data, the first 2D image slice was excluded, equating to about 52 nm of material (see below). This was done to decrease the contribution from surface contamination. For the HMR data, slices 50–130 were summed and displayed to best emphasize the $C_xH_yO_z^-$ intracellular features.

The advantage of using the burst mode instead of the HMR mode is clearly demonstrated in Figure 3. In the HMR mode, the secondary ion signals outline the general shape of the cells, however the exact localization of specific chemical species is difficult to visualize. The $BrdU^-$ signal is detected inside the cell nuclei using both operating modes, although with higher spatial resolution in the burst mode. The $BrdU^-$ image is dominated by the atomic $^{81}Br^-$ secondary ion signal, although the molecular $C_4H_2N_2O_2{}^{79}Br^-$ and $C_4H_2N_2O_2{}^{81}Br^-$ were also included (See Table S-1). These molecular signals were detected in the nucleus in an earlier ToF-SIMS study[64]. The low intensity of these molecular species compared to the atomic $^{81}Br^-$ signal was possibly caused by damage to the molecular species during the C_{60} etching sequences. Higher spatial resolution images of bromine at m/z 81^- could be acquired with a NanoSIMS instrument[62,66], with the tradeoff that only a small number of secondary ions may be followed at once, and must be determined ahead of time. Large GCIB argon clusters reduced the damage during etching in several sample types[67] and would be expected to increase the yields of these molecular fragments.

Comparing the $\Sigma C_xH_yO_z{}^-$ images (See Table S-1 for details of the peaks included in these images) obtained using HMR and burst modes highlight the need for high spatial resolution for optimal ToF-SIMS imaging. The images acquired in the burst mode show the $C_xH_yO_z{}^-$ fragments are located outside of the cells' nuclei in tightly packed bundles (bottom row, fourth column). The 16–84% line scan across one of these features, shown in Figure 4, reveals that the burst mode is capable of spatial resolutions that are at or slightly below a micron (~900 nm) for biological cells. In this case, the ultimate spatial resolution is determined by the intensity and distribution of chemical species imaged, not the beam size, which is focused to ~200nm, or the pixel size, which was 644nm. In contrast, these structures are largely blurred out in the HMR images. In several cells almost the entire cytoplasmic region appears to contain significant $C_xH_yO_z{}^-$ signal. In the burst mode, there are multiple small cavities in the $PO_3{}^-$ image where the phosphate content is significantly lower than in the surrounding area, consistent with a NanoSIMS study that resolved cytoplasmic regions with very low P^- intensity and high CN^- intensity[65]. The sum of $C_xH_yO_z{}^-$ signals is detected around the cells nuclei and is largely located within these cavities. These cavities are not visible in the HMR images. When compared to fluorescence images from the literature, the $C_xH_yO_z{}^-$ enriched regions seem to correspond to the Golgi apparatus of the HeLa cells[65]. As Golgi are composed of stacks of membranous cisternae, it is possible that the $C_xH_yO_z{}^-$ species are fragments of the fatty acids from these cisternae[68]. Further experiments using labels would be necessary to confirm this identification.

The $C_xH_yO_z{}^-$-rich domains may also be due to a fixation artifact as paraformaldehyde molecules could be "trapped" inside the HeLa cells during fixation. Paraformaldehyde is also composed of oxygen, carbon and hydrogen ($OH(CH_2O)_nH$ with n = 8 – 100). A $BrdU^-$ (green) and $C_xH_yO_z{}^-$ (purple) overlay is shown on the far right of Figure 3. It is clear from the burst mode overlay that the structures depicted by the $C_xH_yO_z{}^-$ signals do not extend to large regions of the cytoplasmic space, as is depicted in the HMR overlay. This suggests that these signals arise from a particular type of organelle and not a species common to the entire cytoplasm. The $C_xH_yO_z{}^-$ domains were detected from HeLa cells in multiple samples. However, they were not detected in 3D reconstructions of NIH/3T3 fibroblasts[35].

AFM images of the HeLa cells were also acquired before and after etching (separate data set) with well-defined $C_{60}{}^{q+}$ dose densities. An example of these AFM images is shown in Supplemental Figure S-1. These images were used to calibrate the depth scale of the corresponding 3D reconstructions and to determine average etching rates. By dividing the thicknesses measured by AFM and correlating the data with $C_{60}{}^{q+}$ dose density, an estimation of the sputter rate could be obtained. Supplemental Figure S-2 shows a similar sputter rate for both paraformaldehyde-fixed and freeze-dried cells when using $C_{60}{}^+$ at 10

keV. Linear fits to data gave a sputter rate of 4 nm per 1×10^{13} C_{60}^+ions/cm^2 at 10 keV and 9.5 nm per 10^{13} C_{60}^{++} ions/cm^2 at 20 keV throughout the cells. By using these estimated sputter rates, the C_{60} dose density can be converted to approximately 52 nm removed per C_{60} sputter cycle in the burst mode imaging experiments. Some the cells in the 3D burst mode images are completely etched away after 10 cycles. The maximum height of these cells can then be estimated as 520 nm, which is in good agreement with the values found in Supplemental Figure 2 and those in Robinson *et al.*[35]. For other cells the maximum height is estimated to be larger than 520 nm because more than 10 cycles were needed to completely etch the cellular material. It is interesting to note that the C_{60} etching rates of the HeLa cells used here and NIH/3T3 fibroblasts are quite similar (both ~9 nm per 10^{13} C_{60}^{++} ions/cm^2 at 20 keV), despite being different cell types, and data from both studies indicate that there is little difference in the sputter rate between freeze-dried and chemically fixed cells.

Each voxel of the 3D data sets presented in Figure 3 contains a full mass spectrum, meaning that the data set contains 9.2×10^5 spectra, making it challenging to extract relevant information. This is especially true when all of the stacks are summed and presented in two dimensions. Other ways to present this data are illustrated in Figure 5. The 3D image in the bottom left of Figure 5 shows that the first layer, acquired before C_{60}^+ etching, has a much more intense total ion signal than the rest of the slices. It may be that this is due to surface contamination or residual cell growth media that was removed by the initial C_{60} etching cycle. The apparent size of the cells decreases as the C_{60}^+ dose increases, indicating that a portion of the cell is removed with each successive C_{60} etching sequence. This decrease partially explains why many signals decline slowly with the increasing C_{60}^+ dose during the full depth profiles of cells in Brison *et al.*[64]. Further identification of sub-cellular features in the 3D image of Figure 5 is difficult. An alternative way to present the data for specific ion signals is to show a z-corrected XZ or YZ vertical cross-section, first demonstrated by Breitenstein *et al.*[33,61]. A similar method was later applied to HeLa cells where the cells were reconstructed in 3D and the nucleus was discerned from the cytoplasm using DNA molecular signals and PCA[34]. The z-correction is a simple, yet important transformation that displays the mass spectral distribution of non-flat samples more accurately. The major assumption of this correction is that the sputter rate of the sample remains uniform throughout the acquisition, as is shown in this work and by others[35]. The result of this approach is shown in the right part of Figure 5 for the total negative ion signal, the sum of the $C_xH_yO_z^-$ signals, the sum of the BrdU$^-$ signals, and the Si$^-$ signal from the substrate. Based on the values given above, each cross section is approximately 520 nm high and 165 μm long.

The nuclei of the HeLa cells, indicated by the higher intensity of BrdU$^-$, are clearly defined. They are surrounded by voxels with lower BrdU$^-$ intensity that are interpreted as the cytoplasm. The thickness of the cells then decreases gradually outside of the nuclear region. At its outermost extremity, the cytoplasm is approximately 100 nm thick. High $C_xH_yO_z^-$ signals are detected in regions outside of the cells' nuclei. A low intensity region is observed between the area with high $C_xH_yO_z^-$ signal and the nucleus of some cells. This may be the perinuclear region that is rich in phospholipids, observed with positive secondary ions (Figure 2). Similar cytoplasmic lipid-rich regions have also been observed previously[33,35] and may be a result of highly membranous organelles surrounding the nucleus. Unfortunately, fatty acid peaks like m/z 255$^-$ (16:0) and 281$^-$ (18:1) did not have sufficient secondary ion intensities to produce a useful reconstruction. Perhaps the next-generation GCIB argon sources will be able to provide data with sufficient intensities to do 3D reconstructions of these ions.

A comparison of three dimensional, z-corrected images reconstructed from the burst and HMR imaging modes is shown in Figure 6. An overlay of the BrdU$^-$ and $C_xH_yO_z^-$

fragments from the HMR mode is shown in the bottom left image. Here, the BrdU is easily visualized and localized to the nucleus, but as before, the $C_xH_yO_z^-$ features are not discernible. In the top left a burst mode image plotting the sum of the CN^- and CNO^- fragments clearly shows the location and shape of each cell. In the top right is the burst mode image showing the sum of $C_xH_yO_z^-$ fragments, where the majority of the $C_xH_yO_z^-$ signal is confined to the regions also observed in Figures 3 and 5. In the bottom right is the burst mode image of the $BrdU^-$ signal, which is localized to the nuclei. For the burst mode images, the first slice was excluded for clarity. No smoothing or transparency was applied to the images shown in Figure 6. To accurately visualize the distributions of the $C_xH_yO_z^-$ and $BrdU^-$ species simultaneously, burst mode was required. In the HMR mode, the $BrdU^-$ was localized to the nuclei, but the $C_xH_yO_z^-$ species could not be well discerned. In the HSR imaging mode, the $C_xH_yO_z^-$ fragments were visible, but the $BrdU^-$ fragments could not be separated from the phosphate peaks.

This work has shown the benefit of doing analysis with simultaneous high mass and spatial resolution (burst mode), however this mode is limited in everyday use in the majority of commercially available ToF-SIMS instruments because the primary ion current is very low. A typical current for the burst alignment mode is 0.05 pA, which can produce images with sufficient chemical contrast in a few minutes. For the burst mode, this current is reduced to less than 0.01 pA. Acquisition times increase dramatically (5–10x) compared to the burst alignment HSR imaging mode. The 3D data set shown in this work was acquired in ~1.3 hours, which is quite long considering the data cube only contained 14 slices. Data cubes where 2D images are acquired every ~10 nm (more typical data acquisition conditions) would require over 6 hrs to acquire a 3D dataset from HeLa cells using a 165 μm × 165 μm view of view.

Conclusions

In this study important parameters influencing the quality of ToF-SIMS images of biological cells were investigated. 3D ToF-SIMS data sets of HeLa cells with incorporated BrdU and subcellular spatial resolution were described. High-resolution spectra and images of the HeLa cells were acquired in different LMIG operating modes and were compared. The results show that images acquired with both high mass and spatial resolutions are necessary to properly assign secondary ion species and to image subcellular regions. When using the "burst mode" where the Bi_3^+ beam is not bunched, but contains bursts of short pulses, BrdU-rich nuclei and subcellular regions with high concentration of oxygen containing fragments (i.e., $C_xH_yO_z^-$) were observed. The BrdU and $C_xH_yO_z^-$ regions were also observed in the high mass resolution mode (low spatial resolution), but visualization of their specific location inside the cells was difficult. The sputter rate was observed to be uniform during the C_{60}^+ depth profiling of the cells, allowing a depth scale to be applied to the 3D data cubes, more accurately revealing the locations of the cells' nuclei and of other intracellular species of the HeLa cells.

Supplementary Material

Refer to Web version on PubMed Central for supplementary material.

Acknowledgments

References

1. Belu AM, Graham DJ, Castner DG. Biomaterials. 2003; 24:3635–3653. [PubMed: 12818535]

2. Brunelle A, Touboul D, Laprevote O. J Mass Spectrom. 2005; 40:985–999. [PubMed: 16106340]

3. Castner DG, Ratner BD. Surf Sci. 2002; 500:28–60.

4. Fletcher JS, Henderson A, Biddulph GX, Vaidyanathan S, Lockyer NP, Vickerman JC. Appl Surf Sci. 2008; 255:1264–1270.

5. Vickerman JC. Surf Sci. 2009; 603:1926–1936.

6. Ostrowski SG, Van Bell CT, Winograd N, Ewing AG. Science. 2004; 305:71–73. [PubMed: 15232100]

7. Frisz JF, Choi JS, Wilson RL, Harley BAC, Kraft ML. Anal Chem. 2012; 84:4307–4313. [PubMed: 22507202]

8. Tucker K, Li Z, Rubakhin S, Sweedler J. J Am Soc Mass Spectrom. 2012; 23:1931–1938. [PubMed: 22930440]

9. Appelhans AD, Delmore JE. Anal Chem. 1989; 61:1087–1093.

10. Winograd N. Anal Chem. 2005; 77:142–149.

11. Winograd N, Garrison J. Annu Rev Phys Chem. 2010; 61:305–322. [PubMed: 20055679]

12. Touboul D, Kollmer F, Niehuis E, Brunelle A, Laprevote O. J Am Soc Mass Spectrom. 2005; 16:1608–1618. [PubMed: 16112869]

13. Kollmer F. Appl Surf Sci. 2004; 231–232:153–158.

14. Weibel D, Wong S, Lockyer N, Blenkinsopp P, Hill R, Vickerman JC. Anal Chem. 2003; 75:1754–1764. [PubMed: 12705613]

15. Lee JLS, Ninomiya S, Matsuo J, Gilmore IS, Seah MP, Shard AG. Anal Chem. 2010; 82:98–105. [PubMed: 19957960]

16. Mochiji K, Hashinokuchi M, Moritani K, Toyoda N. Rapid Commun Mass Spectrom. 2009; 23:648–652. [PubMed: 19173223]

17. Ninomiya S, Ichiki K, Yamada H, Nakata Y, Seki T, Aoki T, Matsuo J. Rapid Commun Mass Spectrom. 2009; 23:1601–1606. [PubMed: 19399762]

18. Ninomiya S, Nakata Y, Ichiki K, Seki T, Aoki T, Matsuo J. Nuclear Instruments and Methods in Physics Research Section B: Beam Interactions with Materials and Atoms. 2007; 256:493–496.

19. Matsuo J, Okubo C, Seki T, Aoki T, Toyoda N, Yamada I. Nuclear Instruments and Methods in Physics Research Section B: Beam Interactions with Materials and Atoms. 2004; 219–220:463–467.

20. Fuoco ER, Gillen G, Wijesundara MBJ, Wallace WE, Hanley L. J Phys Chem B. 2001; 105:3950–3956.

21. Anderson HH, Bay HL. J Appl Phys. 1975; 46:2416–2422.

22. Anderson HH, Bay HL. J Appl Phys. 1974; 45:953–954.

23. Bouneau S, Brunelle A, Della-Negra S, Depauw J, Jacquet D, Le Beyec Y, Pautrat M, Fallavier M, Poizat JC, Andersen HH. Physical Review B. 2002; 65:144106.

24. Andersen HH, Brunelle A, Della-Negra S, Depauw J, Jacquet D, Le Beyec Y, Chaumont J, Bernas H. Phys Rev Lett. 1998; 80:5433–5436.

25. Gillen G, Roberson S. Rapid Commun Mass Spectrom. 1998; 12:1303–1312. [PubMed: 9773521]

26. Mahoney C. Mass Spectrom Rev. 2010; 29:247–293. [PubMed: 19449334]

27. Muramoto S, Brison J, Castner DG. Anal Chem. 2012; 84:365–372. [PubMed: 22084828]

28. Gillen G, Fahey A, Wagner M, Mahoney C. Appl Surf Sci. 2006; 252:6537–6541.

29. Shard AG, Havelund R, Seah MP, Spencer SJ, Gilmore IS, Winograd N, Mao D, Miyayama T, Niehuis E, Rading D, Moellers R. Anal Chem. 2012; 84:7865–7873. [PubMed: 22897795]

30. Fletcher JS, Lockyer NP, Vaidyanathan S, Vickerman JC. Anal Chem. 2007; 79:2199–2206. [PubMed: 17302385]

31. Nygren H, Hagenhoff B, Malmberg P, Nilsson M, Richter K. Micros Res Tech. 2007; 70:969–974.

32. Fletcher JS, Rabbani S, Henderson A, Blenkinsopp P, Thompson SP, Lockyer NP, Vickerman JC. Anal Chem. 2008; 80:9058–9064. [PubMed: 19551933]

33. Breitenstein D, Rommel CE, Möllers R, Wegener J, Hagenhoff B. Angew Chem Int Ed. 2007; 46:5332–5335.

34. Fletcher JS, Rabbani S, Henderson A, Lockyer NP, Vickerman JC. Rapid Commun Mass Spectrom. 2011; 25:925–932. [PubMed: 21416529]

35. Robinson MA, Graham DJ, Castner DG. Anal Chem. 2012; 84:4880–4885. [PubMed: 22530745]

36. Rabbani S, Fletcher JS, Lockyer NP, Vickerman JC. Surf Interface Anal. 2011; 43:380–384.

37. Fletcher JS, Henderson A, Biddulph GX, Vaidyanathan S, Lockyer NP, Vickerman JC. Appl Surf Sci. 2008; 255:1264–1270.

38. Fletcher JS, Vickerman JC. Anal Chem. 2012; 85:610–639. [PubMed: 23094968]

39. Kollmer F, Paul W, Krehl M, Niehuis E. Surf Interface Anal. 2013; 45:312–314.

40. Gunnarsson A, Kollmer F, Sohn S, Hook F, Sjovall P. Anal Chem. 2010; 82:2426–2433. [PubMed: 20163177]

41. Touboul D, Roy S, Germain DP, Chaminade P, Brunelle A, Laprevote O. Int J Mass spectrom. 2007; 260:158–165.

42. Benabdellah F, Seyer A, Quinton L, Touboul D, Brunelle A, Laprévote O. Anal Bioanal Chem. 2010; 396:151–162. [PubMed: 19711060]

43. McDonnel LA, Heeren RMA. Mass Spectrom Rev. 2006; 26:606–643.

44. Kurczy ME, Piehowski PD, Parry SA, Jiang M, Chen G, Ewing AG, Winograd N. Appl Surf Sci. 2008; 255:1298–1304. [PubMed: 19554199]

45. Kurczy ME, Piehowsky PD, Willingham D, Molyneaux KA, Heien ML, Winograd N, Ewing AG. J Am Soc Mass Spectrom. 2010; 21:833–836. [PubMed: 20219392]

46. Barnes CA, Brison J, Robinson M, Graham DJ, Castner DG, Ratner BD. Anal Chem. 2011; 84:893–900. [PubMed: 22098081]

47. Muramoto S, Brison J, Castner DG. Surf Interface Anal. 2011; 43:58–61. [PubMed: 22016576]

48. Robinson M, Castner D. Biointerphases. 2013; 8:15.

49. Jones EA, Lockyer NP, Vickerman JC. Anal Chem. 2008; 80:2125–2132. [PubMed: 18278949]

50. Carado A, Kozole J, Passarelli M, Winograd N, Loboda A, Wingate J. Appl Surf Sci. 2008; 255:1610–1613.

51. Carado A, Passarelli MK, Kozole J, Wingate JE, Winograd N, Loboda AV. Anal Chem. 2008; 80:7921–7929. [PubMed: 18844371]

52. Smith D, Kiss A, Leach F III, Robinson E, Paša-Toliæ L, Heeren RA. Anal Bioanal Chem. 2013; 405:6069–6076. [PubMed: 23685962]

53. Smith DF, Robinson EW, Tolmachev AV, Heeren RMA, Paša-Toliæ L. Anal Chem. 2011; 83:9552–9556. [PubMed: 22060180]

54. HR2 Molecular Imaging of Organic Droplet Defects with the New PHI Cluster LMIG. Physical Electronics; Chanhassen, Minnesota: 2013.

55. Havercroft, N. Personal communication. Annapolis, MD: 2013. IONTOF Gmbh.

56. Brison J, Muramoto S, Castner DG. J Phys Chem C. 2010; 114:5565–5573.

57. Taupin P. Brain Res Rev. 2007; 53:198–214. [PubMed: 17020783]

58. Zhu Z, Shutthanandan V, Engelhard M. Surf Interface Anal. 2012; 44:232–237.

59. Malm J, Giannaras D, Riehle MO, Gadegaard N, Sjövall P. Anal Chem. 2009; 81:7197–7205. [PubMed: 19639962]

60. Berman ESF, Fortson SL, Checchi KD, Wu L, Felton JS, Wu KJJ, Kulp KS. J Am Soc Mass Spectrom. 2008; 19:1230–1236. [PubMed: 18565760]

61. Breitenstein D, Rommel CE, Stolwijk J, Wegener J, Hagenhoff B. Appl Surf Sci. 2008; 255:1249–1256.

62. Frisz JF, Lou K, Klitzing HA, Hanafin WP, Lizunov V, Wilson RL, Carpenter KJ, Kim R, Hutcheon ID, Zimmerberg J, Weber PK, Kraft ML. Proc Natl Acad Sci USA. 2013

63. Mantus DS, Ratner BD, Carlson BA, Moulder JF. Anal Chem. 1993; 65:1431–1438. [PubMed: 8517550]

64. Brison J, Benoit DSW, Muramoto S, Robinson M, Stayton PS, Castner DG. Surf Interface Anal. 2011; 43:354–357. [PubMed: 22058579]

65. Römer W, Wu TD, Duchambon P, Amessou M, Carrez D, Johannes L, Guerquin-Kern JL. Appl Surf Sci. 2006; 252:6925–6930.

66. Gutleb A, Freitas J, Murk A, Verhaegen S, Ropstad E, Udelhoven T, Hoffmann L, Audinot JN. Anal Bioanal Chem. 2012; 404:2693–2698. [PubMed: 22566200]

67. Rabbani S, Barber AM, Fletcher JS, Lockyer NP, Vickerman JC. Anal Chem. 2011; 83:3793–3800. [PubMed: 21462969]

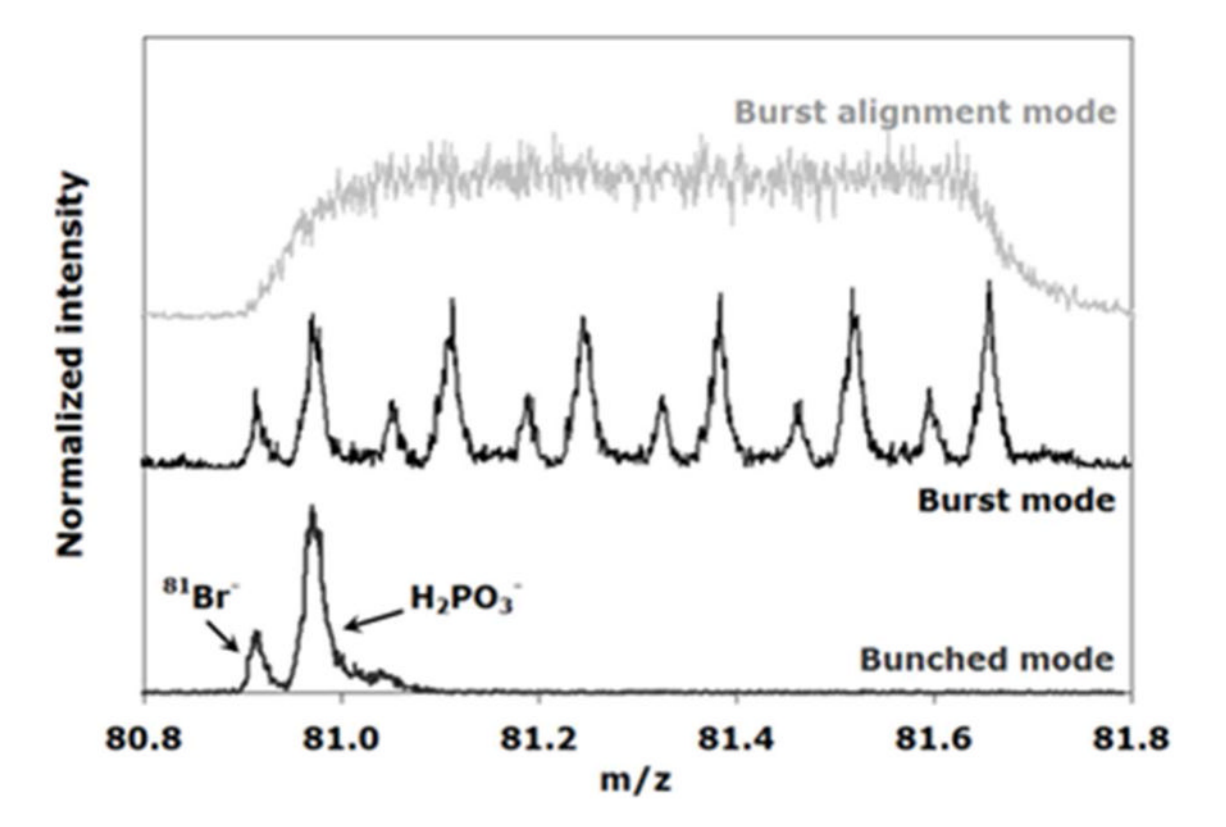68. Magnusson YK, Friberg P, Sjovall P, Malm J, Chen Y. Obesity. 2008; 16:2745–2753. [PubMed: 18833214]

Figure 1.
Three Bi_3^+ analysis modes used for ToF-SIMS analysis of HeLa cells treated with BrdU generate different spectra. Top spectrum: HSR "burst alignment" mode. Middle spectrum: "burst" mode with both high mass and spatial resolutions. Bottom spectrum: HMR "bunched" mode. Additional details of the analysis modes are provided in the experimental section.
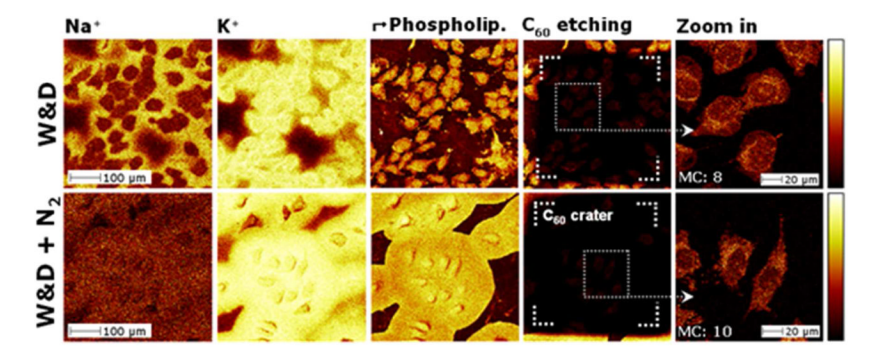
Figure 2.
Positive burst alignment (HSR) ion images of the HeLa cells prepared by a simple wash-and-dry method. The cells were rinsed with AA and then dried in air (top row) or with a gentle flow of N_2 (bottom row). Etching was performed using C_{60}^{++} at 20 keV with a dose of 1.0×10^{14} C_{60}^{++} ions/cm^2.
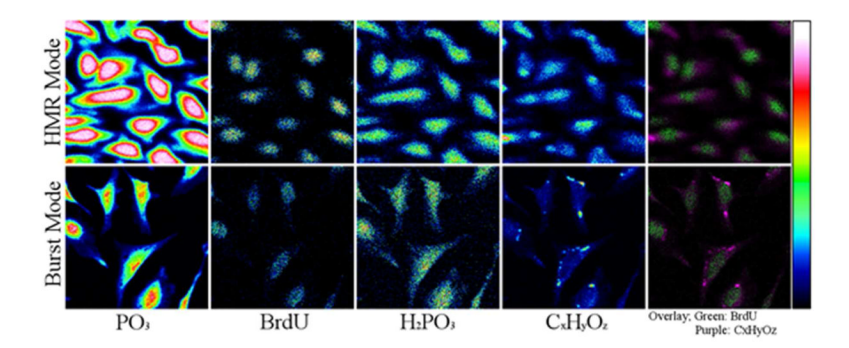
Figure 3.
ToF-SIMS images (Left to right: PO_3^-, $BrdU^-$, $H_2PO_3^-$, $C_xH_yO_z^-$ and an overlay of $BrdU^-$ and $C_xH_yO_z^-$) of HeLa cells acquired from the same sample in HMR mode (top row) and burst mode (bottom row). The images were reconstructed by summing multiple images from the 3D data stack. The images in the top row are 202×202 μm^2 and the images in the bottom row are 165×165 μm^2.
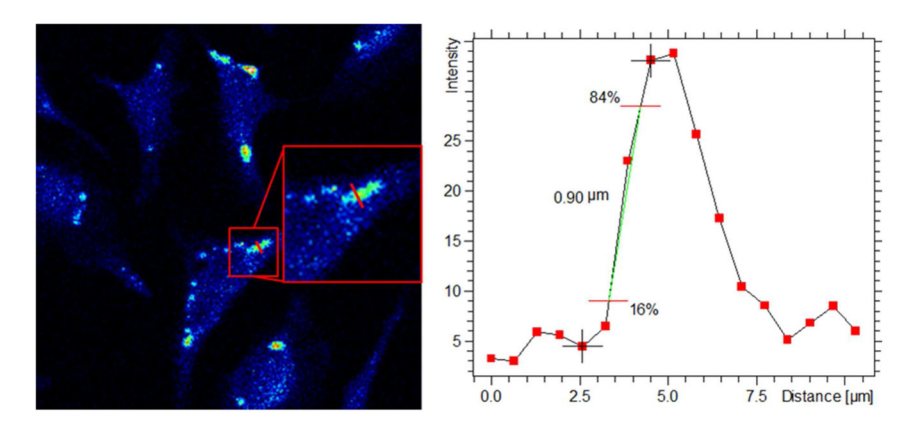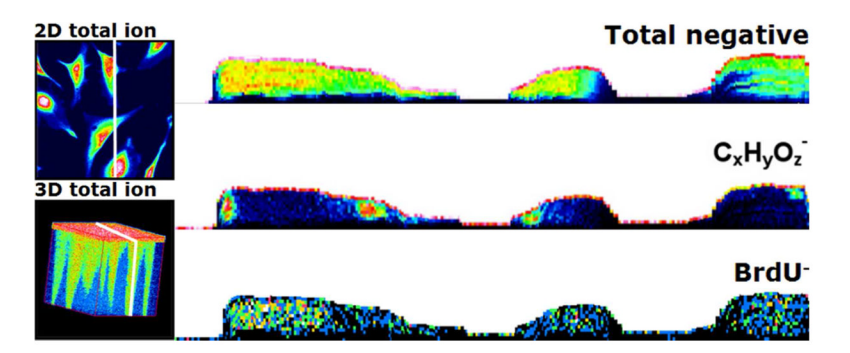
Figure 4.
Left image: Burst mode image of the summed $C_xH_yO_z^-$ species from Figure 3. Inset: Blow up of the portion in the red box. Right image: Line scan across the red line in the left image. The line scan shows that sub-micrometer spatial resolution was achieved using burst mode to collect data from single HeLa cells.

Figure 5.
Negative ToF-SIMS images of HeLa cells. Top left: 2D image (total ion) obtained by summing the images from all 14 slices. Bottom left: 3D total negative ion image showing the 14 analysis/etching cycles. This 3D image was not z-corrected. Right: vertical cross-sections for specific ion signals after the z-correction. The position of the vertical cross-section is shown by the white lines in the 2D and 3D images.
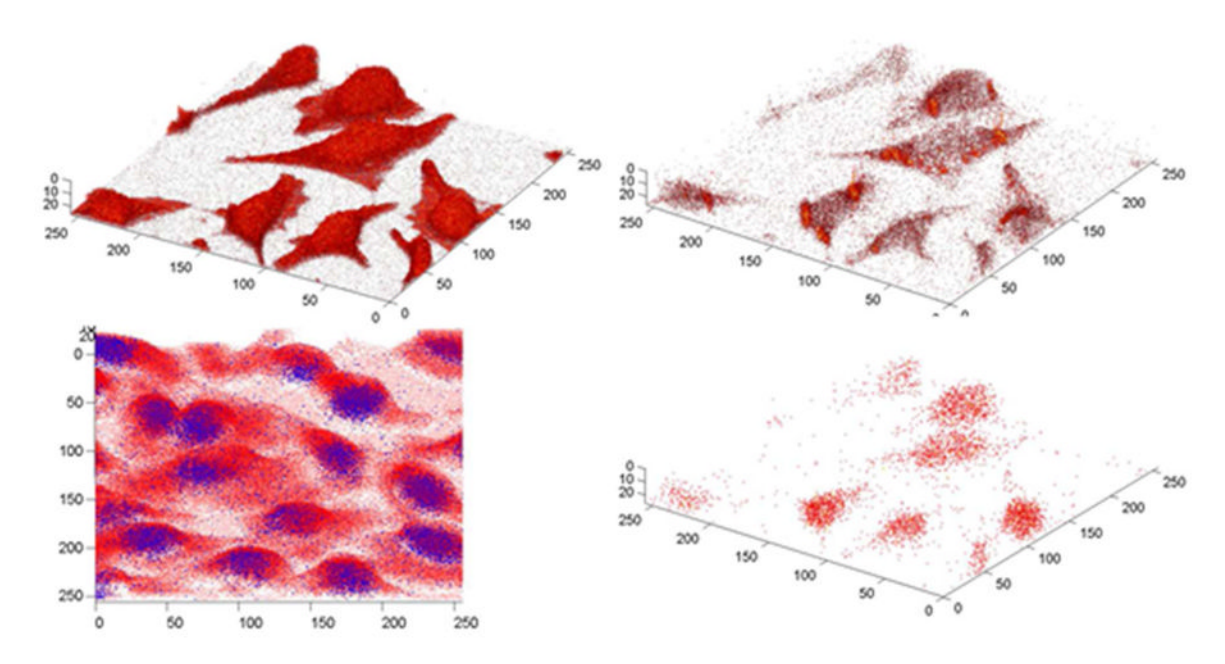
Figure 6.
Z-corrected 3D images of BrdU localized within cells using two different LMIG operating modes. In the bottom left overlay is obtained from the HMR bunched mode with the BrdU$^-$ signal shown in blue and the sum of the $C_xH_yO_z^-$ signals in red. The other three images are burst mode images. The top left: CN$^-$ + CNO$^-$; top right: $\Sigma C_xH_yO_z^-$; bottom right: ΣBrdU$^-$. The bottom left image is $202 \times 202 \ \mu m^2$ and contains 24 slices. The burst mode images are $165 \times 165 \ \mu m^2$, and contain 26 slices.